Eur. Phys. J. A (2015) **51**: 93
DOI 10.1140/epja/i2015-15093-0

THE EUROPEAN PHYSICAL JOURNAL A

Special Article – Tools for Experiment and Theory

Improvements in data analysis obtained by large-area silicon ΔE-E detector telescopes

M. Uroić[1,a], M. Milin[2], A. Di Pietro[3], P. Figuera[3], M. Fisichella[3], M. Lattuada[3,4], I. Martel[6], Đ. Miljanić[1], M.G. Pellegriti[3], L. Prepolec[1], A.M. Sánchez Benítez[6,7], V. Scuderi[3], N. Soić[1], E. Strano[3,5], and D. Torresi[3,5]

[1] Ruđer Bošković Institute, Zagreb, Croatia
[2] Department of Physics, Faculty of Science, University of Zagreb, Zagreb, Croatia
[3] INFN-Laboratori Nazionali del Sud, Catania, Italy
[4] Dipartimento di Fisica e Astronomia Universtita' di Catania, Catania, Italy
[5] INFN-Laboratori Nazionali di Legnaro, Legnaro, Italy
[6] Departamento de Fisica Aplicada, Universidad de Huelva, Huelva, Spain
[7] Centro de Física Nuclear da Universidade de Lisboa, 1649-003 Lisboa, Portugal

Received: 12 March 2015 / Revised: 23 June 2015
Published online: 3 August 2015 – © Società Italiana di Fisica / Springer-Verlag 2015
Communicated by D. Pierroutsakou

Abstract. The paper describes a few practical methods for the analysis of data obtained by standard thin-thick silicon detector telescopes used in nuclear reaction measurements. The addressed issues are: 1) improvement in double-sided silicon strip detector (DSSSD) calibration based on the fact that each event is registered twice, both in horizontal and vertical strips, 2) improvements in particle identification and 3) simplified mapping of the non-uniformity of the thin detector, without a dedicated measurement of the thickness. The proposed procedures are applied on experimental data obtained for 30 MeV ^{7}Li beam induced reactions on LiF and C targets, studied with a detection setup consisting of four telescopes placed at different angles and distances. The proposed methods aim at quicker and more reliable calibration and particle identification.

1 Introduction

Modern experimental nuclear physics research becomes more and more based on measurements using highly segmented semiconductor detector setups, usually covering a significant part of the full solid angle. This enables measurements of rather small yields *e.g.* of reactions induced by low-intensity radioactive beams, but also presents a demanding task in on-line and off-line analysis. Features associated with detector dead layer [1] or inter-strip gaps [2,3] are only part of the problem, the very basic one being the calibration of a large number of (apparently) independent detector channels.

The DSSSDs are usually rather large (*e.g.* 5 cm×5 cm), segmented on both sides and nowdays commercially available in different thicknesses. In our measurement, four telescopes were used, each consisting of a thick detector (one of 500 μm and three of 1000 μm) and a thin one (67, 57, 64 and 59 μm), all $5\times5\,\mathrm{cm}^2$, supplied by Micron Semiconductors. Thick detectors were 16 + 16 strip DSSSDs, whereas the thin ones were divided in four square quadrants. A more detailed description of DSSSD properties is given, *e.g.* in [3]. The data acquisition system consisted of 16-channel Mesytec preamplifiers, 16-channel Silena amplifiers, 32-channel CAEN peak-sensitive ADC-s and a computer for recording and storing the events.

When used in detector telescopes to provide charged particle identification via the ΔE-E method, energy calibration of each detector is not at all trivial and usually very time-consuming. This article discusses several improvements which can make the calibration easier, faster and more precise.

2 Relative calibration of strips in DSSSD

DSSSDs are designed to record the ion impact position and energy by registering the produced charge both on the front and back sides. The position is then reconstructed from the *pair* of channels which record the event, with their intersection pixel nominated as position. For example, the present 16 + 16 strip array is giving 256 pixel resolution (fig. 1(a)).

However, an additional bonus is the double acquisition of the *energy signal* of the particle. This is routinely used to verify the proper energy deposition and exclude

[a] e-mail: milivoj.uroic@irb.hr

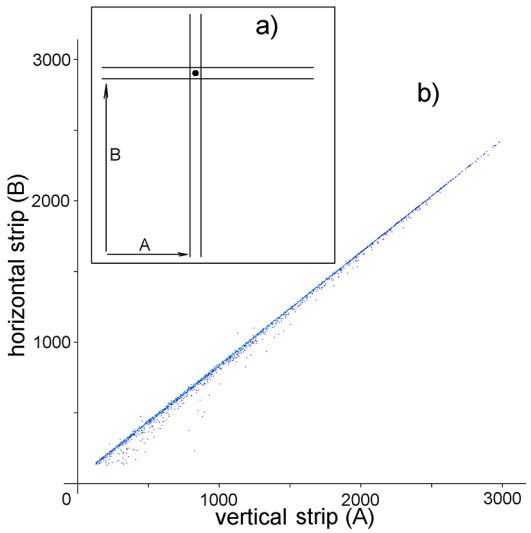

Fig. 1. Position in DSSSDs is defined as the pixel at the intersection of the two strips (A, B) which recorded the impact. The energy readout values are linearly correlated, since they are produced by the same charge collection, thus the correct events, regardless of origin, are located on a straight line.

or mark interstrip events or noise, but it can be very useful in calculating the majority of calibration parameters (those which are independent of particle types, energy, angle, kinematics) and improving its quality. Figure 1(b) displays typical uncalibrated energy readout of a horizontal *vs.* a vertical strip. The proposed calibration procedure starts by correlating these value-pairs by a linear fit of the data shown in fig. 1(b). Such a fit covers the whole measured energy range, and has good statistics, with all the correct events in each pixel included.

Knowing all energy correlations between strips, it is possible to reduce the number of unknown calibration parameters from $2 \times 2 \times 16$ to only 2. In other words, this answers the following question: "If one knows the calibration of one strip, can the redundant energy-signal record be used to calculate calibration of all the other strips in that detector?"

The proposed procedure is the following: One strip, *e.g.* first vertical, and its uncalibrated energy spectrum is used "as a reference" for the relative calibration. If one plots the data of this strip *vs.* all the horizontal strips, 16 spectra similar to the one shown in fig. 1(b) are obtained, producing 16 least-square linear fits for each pixel of the reference strip. The obtained coefficients (given in table 1, right part) are used to relate energy signal of each horizontal strip to the energy signal of the reference strip. As this is independent of the spectrum features, it is done for all events which include the reference strip, without having to identify them. In the second stage, the coefficients of all vertical strip except the referent are calculated. This is done using all the events *except* the events in the reference strip. During this second stage, horizontal strip data is related to the reference strip value, using the coefficients obtained from the first stage. This enables the intersecting vertical strips to be compaired against the reference strip

Table 1. An example of relative calibration: coefficients for detector 3.

ch. front vertical	k	l
01	1.00000	0.000
02	1.00020	−36.545
03	1.01873	10.703
⋮	⋮	⋮
15	1.07443	−37.270
16	1.04468	−20.381

ch. back horiz.	k	l
17	1.25506	−54.017
18	1.22056	−70.398
19	1.29202	−67.921
⋮	⋮	⋮
31	1.26313	−81.660
32	1.26752	−88.916

value, and the least-square linear fit again produces the coefficients in the left half of table 1.

A similar procedure known as gain-matching is often used for preliminary on-line analysis and presentation of data. The main improvement here is the fact that we do not compare any features (like calibration peaks) that depend on identification and peak-fitting, but make use of the most part of acquired data, regardless of identifying their origin.

This procedure results in a table like table 1, which relates all the channel values to the channel value in the reference strip, *i.e.* $x_1 = k_n x_n + l_n$.

The table was recalculated for different reference strips, and again for different datasets (different runs) acquired during the experiment. This enables one to check if the acquisition chain gain (detector, preamp, amplifier, ADC) drifted during the experiment, as the values should be the same for the first and last run. No significant gain drifting was found during this measurement, *i.e.* differences between runs were non-systematic and within 1.6 channels ($\leq 30\,\mathrm{keV}$).

The whole detector can now be calibrated at once, as these coefficients enable us to compare the strips directly. In this case, the calibration was determined by elastic scattering peaks of 30 MeV ^{7}Li ion beam on gold and carbon targets, using all such events in one telescope. The energy of elastic scattering events differs with the scattering angle, which was calculated for each pixel. In the presented case, the resulting coefficients were $a = 16.983 \pm 0.072\,\mathrm{keV/channel}$, $b = -970 \pm 19\,\mathrm{keV}$.

The energy in the reference strip is simply calculated as

$$E = a * x + b,$$

and, in all strips, including the reference strip it is given by

$$E_n = a * x_1 + b = a * (k_n x_n + l_n) + b.$$

The advantages of the proposed calibration procedure are:

1) All the strips are aligned in energy since the dispersion due to differences in the calibration is reduced compared to independent channel fitting.

2) If one wants to correct the calibration, it is enough to change only two parameters, a and b.
3) In calculating the parameters k_i and l_i high statistics with all events is achieved.

The same procedure was performed for all four detectors in this experiment, giving the values like in table 1. The values were constant for different runs within four significant digits, which is close to one-channel precision on 4096 channel ADCs, which is substantially more accurate than the physical energy resolution, *i.e.* coefficients a, b.

3 Fine-tuning charged particle identification

With the aim to improve identification of different isotopes, a standard linearization procedure for ΔE-E spectra was slightly modified. Energy calibration of the thin detectors was performed using the same elastic scattering measured with and without the thin detectors in place. The data obtained from 30 MeV and 51 MeV ^{7}Li beam on ^{7}LiF, ^{6}LiF, C and Au targets were checked for consistency in all four detector telescopes, and 51 MeV ^{7}Li beam on ^{7}LiF target data recorded in telescope 2 (at 20°) was chosen to represent the procedure described here. In further text, E stands for the calibrated energy of the thick, ΔE for the thin detector, with $E_b = E + \Delta E$ being their sum used in the inclusive spectra.

Instead of using a standard graphical cut on a ΔE-E plot from raw data, a slowly energy varying function E_f was chosen instead of ΔE,

$$E_f = \sqrt{\Delta E \cdot E + \alpha \Delta E^2} + \beta E, \tag{1}$$

with dimensionless constants $\alpha = 0.7$ and $\beta = 0.05$ chosen to produce values E_f as constant as possible for different energies of the same nuclei [4]. The above-defined E_f has the dimension of an energy and can be expressed in MeV, as E and ΔE. Figure 2 illustrates a comparison between standard ΔE-E plot (a) and E_f-E plot (b), demonstrating nearly constant E_f values for specific nuclei.

A similar linearization technique was developed by the FAZIA group [5,6], with quantitative results presented by *Figure of Merit* (FoM), defined in [7]. However this one differs both in aim and method. Instead of using a numerical procedure based on graphical identification of the data locus, a simple analytical function related to the stopping power properties was preferred. The method presented here is less general, but simpler for this specific use. The aim of this step, in addition to quantifying the isotope separation is to *improve* it, using the data to compensate for the thickness variations of the thin detector.

The motivation for the chosen function is the following: to a crude approximation the energy loss in an infinitesimally thin silicon layer for a given nucleus is inversely proportional to particle energy, *i.e.* $\mathrm{d}E \cdot E = \text{const}$ [8]. If the thin-detector thickness were sufficiently small, the choice for E_f would be a simple square root of the product: $E_f = \sqrt{\Delta E \cdot E}$. The main deviation from this expression originates in the finite thickness of the thin detector.

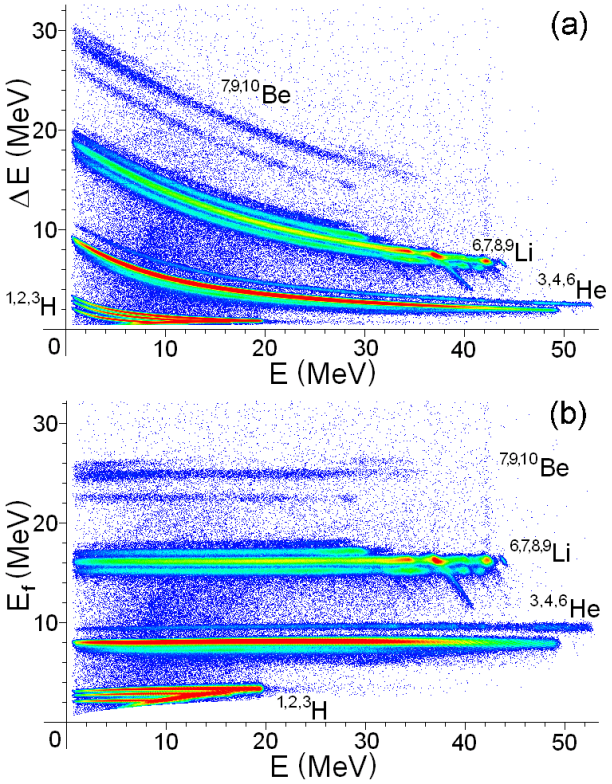

Fig. 2. Standard ΔE-E plot (a) compared with the proposed E_f-E plot (b) for particle identification. Data from 51 MeV ^{7}Li beam on ^{7}LiF target, measured at $20 \pm 5°$.

The expression is thus improved if we integrate the product value from E to $\Delta E + E$, *i.e.* over the energy interval in the thin detector,

$$E_f^2 = \int_E^{\Delta E + E} E \cdot \mathrm{d}E = \frac{(\Delta E + E)^2}{2} - \frac{E^2}{2} = \Delta E \cdot E + 0.5 \Delta E^2. \tag{2}$$

This already gives a nearly constant E_f value for the measured energy range. Further analyzing the obtained plot showed empirically that 0.7 is a better choice than the 0.5 factor obtained from integration, with a slight almost-linear residual energy dependence which was compensated by introducing a linear factor βE, with $\beta = 0.05$.

To summarize, we use eq. (1) with parameters $\alpha = 0.7$ and $\beta = 0.05$, instead of "theoretical" values $\alpha = 0.5$ and $\beta = 0$. This choice appears to be near-optimal for the four 60 μm silicon thin detectors, but other choices are possible.

Reasons for using the proposed E_f expression are: 1) graphical cuts follow almost linear shapes. As the standard graphical cutting tools usually provide segmented (polygon) line data cuts, the graphical cut accuracy is improved simply by following less curved lines, *e.g.*, ^{3}He and ^{4}He separation. 2) as it will be discussed in the next section, further improvement was achieved by compensating the non-uniformity of the thin-detector thickness, using the E_f values, with the improvement independent of cuts, and thus quantitatively expressed.

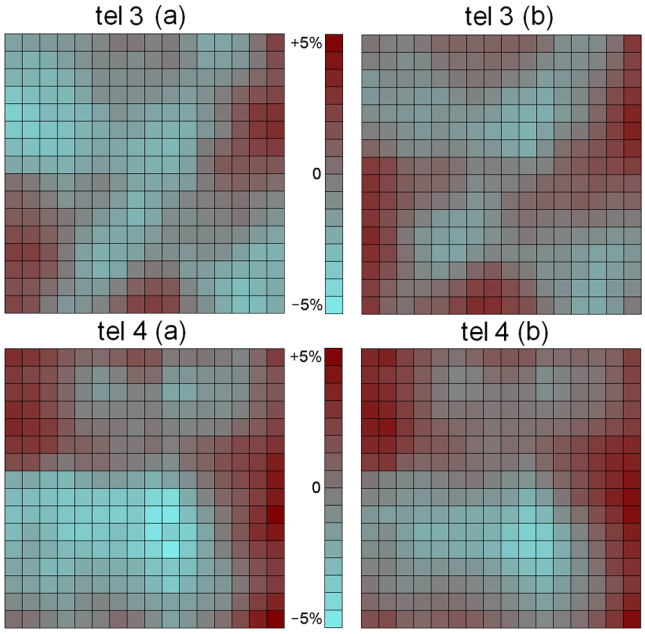

Fig. 3. Thin-detector thickness deviations from average value for two detectors obtained from the ^{7}Li beam run (a) and from the ^{10}B beam run (b) with the same thin detectors. The 16 by 16 grid is the position within the telescope, measured by the DSSSD behind the thin detector.

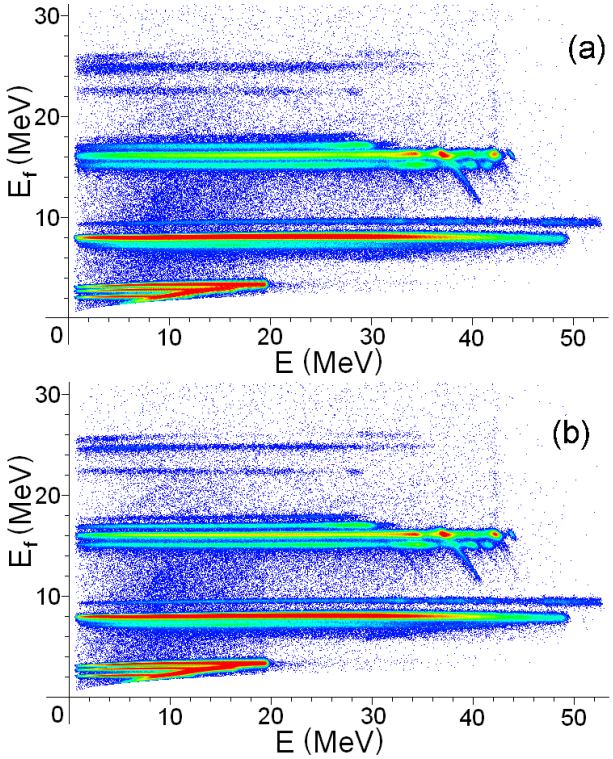

Fig. 4. Unscaled (a) and scaled (b) E_f-E plot of reaction products for ^{7}Li beam on ^{7}LiF target at 51 MeV beam energy.

4 Thickness non-uniformity of the thin detectors

The nearly constant E_f value allows to select a significant energy region of some abundant reaction products (in this case, very abundant α particles on fig. 2) in which the deviation from E_f value has the smallest energy dependence. The E_f value showed a pronounced *position* dependence, *i.e.* it was correlated with the pixel position behind the thin detector. This implied that the recorded energy in the thin detectors was different for different parts of the detector, suggesting thickness variations in thin detectors. Such thickness non-uniformity of the thin detector has already been reported [9,10].

An alpha-particle events selection ($E_f = 8 \pm 0.3$ MeV, $E = 10 \pm 2$ MeV) was done for each pixel. In this region the E_f value for alpha-particles showed the least energy dependence, with high abundance of events. The mean value E_f was calculated for events registered in this energy window. The deviation of E_f from the detector's average was chosen to represent the variation of thickness, with two strong arguments supporting that conclusion, based on the result shown in fig. 3: i) the deviation varies smoothly through the neighboring pixels, ii) the same patterns were found in another measurement with the same thin detectors and ^{10}B beam at 72 MeV energy, with different detector positions and targets.

Other two detector telescopes used in both measurements show similar patterns. The observed thickness variation is larger and different than that due to the difference in incident angle of the incoming particles. The maximal inclination angle for the nearest detector was $\approx 9°$, which produces a maximal effect of 1.2% on thickness, or 0.6% deviation from the average.

With this procedure it is not possible to determine if the average thickness corresponds to the nominal thickness of the detector, or exact thickness variations in μm. However, the impact on the particle identification is represented and calculated through the thickness deviation from other parts of the same detector, *i.e.* relative deviation from the mean value. The impact on the *energy resolution* is small if the calibration is exact, because extra thickness in thin detector merely adds to the deposited energy in the thin, and reduces energy in the thick detector by the same amount.

In the E_f-E plots, the E_f value in each pixel was scaled according to the mean value of the deviation presented in fig. 3 (*i.e.* divided by the ratio of the pixel value and the mean value for the detector), in order to improve the particle identification. The typical result is presented in fig. 4(b), compared to the non-scaled values on fig. 4(a). In order to see the small but important difference, a projection of a slice on E_f axes (fig. 5) shows the improvement in separating the isotopes (fig. 5(a) without scaling, (b) with scaling).

As can be seen from figs. 4 and 5, resolution is improved for *all* nuclei, not just on the alpha-particles for which it was calculated, thus confirming the assumption that the spread has a thickness-based component. Most apparent, the separation of lithium isotopes (6,7,8,9) has improved (aside from visual comparison), FWHM for ^{7}Li has decreased from 0.660 to 0.428 MeV in E_f.

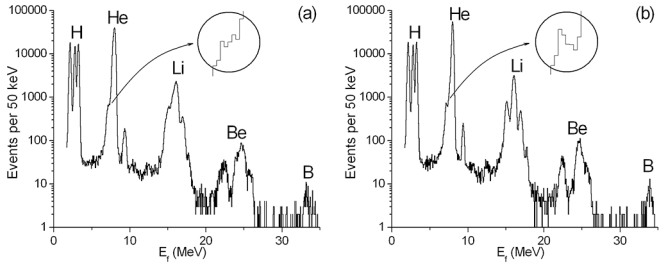

Fig. 5. Projections of fig. 4 data slice (8–12 MeV E) on the E_f-axis: unscaled (a) and scaled (b). The improvement in isotopic separation is best seen on ^{3}He peak (enlarged circle) and lithium isotopes.

The corresponding decrease in ^{6}Li FWHM was from 0.622 to 0.461 MeV. With the peaks 0.91 MeV apart, this equals Figure of Merit (FoM) [7] increase from 0.71 to 1.02, which is estimated to reduce the ratio of ^{7}Li misidentified as ^{6}Li from 5.4% to 1.1% (asymmetric abundance). The less noticeable but equally important is the improved separation between ^{3}He and alpha-particles, shown in enlarged circles.

It is evident that any selection criteria based on corrected data (figs. 4(b) and 5(b)) is more accurate than on uncorrected data (figs. 4(a) and 5(a)). In the following section, the data based on ^{3}He, ^{4}He and ^{6}He isotopes detection are presented, demonstrating a rather clear separation.

5 Inclusive spectra

Using the calibration technique and selection criteria described above, excitation energy spectra for ^{10}Be, ^{20}Ne and ^{15}N were produced, using a 30 MeV ^{7}Li beam on ^{6}LiF, ^{7}LiF and C targets and detecting the outgoing He isotopes.

The excitation spectra of the undetected nucleus, shown in fig. 6 were reconstructed event-by-event using the non-relativistic energy and momentum conservation contained in the following collision kinematics formula for the general two-body reaction $A(a,b)B^*$:

$$E^* = Q_0 + \frac{m_B - m_a}{m_B}E_a - \frac{m_B + m_b}{m_B}E_b + \frac{2}{m_B}\sqrt{m_a m_b}\sqrt{E_a E_b}\cos\theta_b,$$

with m_A, m_B, m_a and m_b being mass of the corresponding nucleus in a.m.u., Q_0 the Q-value for the reaction to the ground state, E_a the beam energy, and E_b, θ_b the energy and scattering angle of the recorded nucleus b, in the laboratory frame.

Published results on levels and reactions [11–13] were used to identify the peaks, and estimate systematic (δE) error. Gaussian standard deviation $\sigma = \mathrm{FWHM}/\sqrt{8\ln 2}$ was obtained from the least-square fit of the peaks. It should be noted that covering large solid angles with a single detector generally improves statistics, but enhances

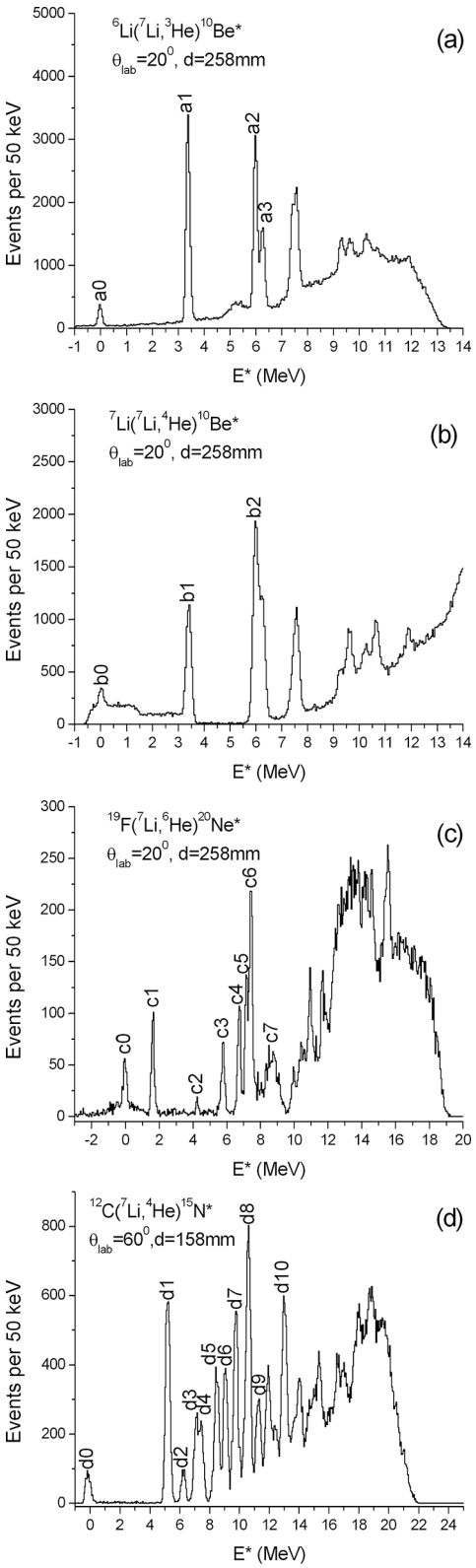

Fig. 6. Excitation energy spectra of ^{10}Be, ^{20}Ne and ^{15}N obtained with a ^{7}Li 30 MeV beam. Telescopes cover ±5.5° (a)–(c) and ±9.0° (d) range around the mean scattering angle θ_{lab}. See text for details.

Table 2. Comparison of peak energies $E_{\rm fit}$ with TUNL [11–13] values $E_{\rm TUNL}$ and corresponding difference δE. Peak widths are expressed in standard deviation $\sigma(E)$. All energies are given in keV.

Peak	$E_{\rm fit}$	$E_{\rm TUNL}$	δE	$\sigma(E)$
a0	−40	0	−40	84
a1	3349	3368	−19	78
a2	5965	5960	+5	81
a3	6240	6180	+60	–
b0	−11	0	−11	99
b1	3388	3368	+20	95
b2	5994	5960	+34	–
c0	−33	0	−33	97
c1	1620	1634	−14	95
c2	4267	4248	+19	74
c3	5778	5788	−10	83
c4	6741	6725	+16	79
c5	7172	7156	+16	–
c6	7436	7422	+14	90
c7	8697	≈ 8700	–	319
d0	−110	0	−110	142
d1	5165	5290	−125	135
d2	6217	6328	−111	125
d3	7100	7160	−60	–
d4	7450	7570	−120	–
d5	8463	8577	−114	129
d6	9044	9161	−117	126
d7	9756	9818	−62	137
d8	10567	10521	46	137
d9	11265	11274	−9	148
d10	12994	13002	−8	147

the errors due to angular resolution. Forward placed detectors (smaller scattering angle θ) produce better resolution due to smaller angle-energy dependance and were in this case put further from the target. Excitation energy spectra obtained for reactions on ^{6}Li, ^{7}Li, ^{12}C and ^{19}F target nuclei are presented. In LiF targets, states from reactions on lithium and fluorine sometimes overlap, but for the non-assumed target nucleus, the incorrect kinematical assumption spreads the events for different detection angles, instead of producing a peak. As the detector cover a large scattering angle, the spread of non-assumed event is quite large, merely modifying the continuum background.

Table 2 quantifies the relevant errors for comparison. Although the quality of the spectra depends on many factors, the described method enables to minimize the errors due to independent treatment of individual segments of the detector, which makes the quality of the shown spectra similar to single-channel small-area detectors.

The spectra for the reactions ^{6}Li(^{7}Li, ^{3}He)^{10}Be and ^{7}Li(^{7}Li, ^{4}He)^{10}Be shown in fig. 6(a) and 6(b) show a state at $E^{*} \approx 10.15\,$MeV, which is almost never seen in single spectra (exceptions being only those in refs. [14] and [15]), due to its peculiar structure [16,17]. The spectrum on fig. 6(a) has clearly resolved doublet of states at $E^{*} = 5.96\,$MeV and $6.18\,$MeV —this is again a feature rarely seen in single spectra obtained by silicon detector telescopes.

Spectra on panels (c) and (d) of fig. 6 are obtained on ^{12}C and ^{19}F target nuclei. Their quality is comparable with those obtained measuring the same reactions with the small silicon ΔE-E telescopes (refs. [18] and [19], respectively).

6 Summary

Low energy nuclear physics experiments become more and more complex as the number of used detector channels increases, which also makes time required for analysis significantly longer. Here, three recipes are proposed on how to make the analysis simpler, faster and more accurate. The first one describes fast relative calibration of both vertical and horizontal strips of a DSSSD. The second one improves the standard ΔE-E method of particle identification in a way that simplifies making of graphical cuts. Finally, the last recipe shows a method to deal with ΔE-detector non-uniformities if any part of the telescope gives information of the position of detected particle, eliminating the need for separate measurement of the thickness. The value of the proposed improvements is demonstrated on experimental data from the ^{7}Li + ^{6,7}LiF measurement (at 30 MeV), giving some of the best excitation energy spectra obtained by large area silicon detectors for ^{10}Be, ^{15}N and ^{20}Ne. We believe that the proposed methods can be useful for the low-energy nuclear physics community, since they could be applied to some of the many similar experiments being performed.

The support to this work was provided by the Ministry of Science, Education and Sports of the Republic of Croatia. The authors from Catania acknowledge the partial financial support of the Italian Ministry of Education and Research (PRIN 2010-2011, project 2010 TPSCSP).

References

1. O. Tengblad *et al.*, Nucl. Instrum. Methods A **525**, 458 (2004).
2. D. Torresi *et al.*, Nucl. Instrum. Methods A **713**, 11 (2013).
3. L. Grassi *et al.*, Nucl. Instrum. Methods A **767**, 99 (2014).
4. M. Uroić *et al.*, AIP Conf. Proc. **1491**, 357 (2012).
5. FAZIA Collaboration (L. Bardelli *et al.*), Nucl. Instrum. Methods A **654**, 272 (2011).
6. FAZIA Collaboration (N. Le Neindre *et al.*), Nucl. Instrum. Methods A **701**, 145 (2013).
7. R.A. Winyard, J.E. Lutkin, G.W. McBeth, Nucl. Instrum. Methods **95**, 141 (1971).
8. H. Bethe, Ann. Phys. **397**, 325 (1930).

9. B. Davin *et al.*, Nucl. Instrum. Methods A **473**, 302 (2001).
10. T. Paduszynski *et al.*, Nucl. Instrum. Methods A **547**, 464 (2005).
11. D.R. Tilley *et al.*, Nucl. Phys. A **745**, 155 (2004).
12. F. Ajzenberg-Selove, Nucl. Phys. A **523**, 1 (1991).
13. D.R. Tilley *et al.*, Nucl. Phys. A **636**, 249 (1998).
14. Y.A. Glukhov *et al.*, Sov. J. Nucl. Phys. **13**, 154 (1971).
15. S. Hamada *et al.*, Phys. Rev. C **49**, 3192 (1994).
16. M. Milin *et al.*, Nucl. Phys. A **753**, 263 (2005).
17. M. Freer *et al.*, Phys. Rev. Lett. **96**, 042501 (2006).
18. M.E. Williams-Norton *et al.*, Phys. Rev. C **12**, 1899 (1975).
19. C. Lee *et al.*, Phys. Rev. C **60**, 024317 (1999).